Seventh International Conference on Computational Fluid Dynamics (ICCFD7), Big Island, Hawaii, July 9-13, 2012

ICCFD7-3703

Numerical simulations of two-dimensional turbulent thermal convection on the surface of a soap bubble

Y-L. Xiong, P. Fischer and C-H. Bruneau
Corresponding author: patrick.fischer@math.u-bordeaux1.fr
Univ. Bordeaux, IMB. CNRS UMR 5251. INRIA Bordeaux Team MC2. F-33400 Talence, France

Abstract: We present in this paper an original method to implement cartesian computations to solve a spherical problem. The problem consists in performing the numerical simulations of a half bubble of soap located on a heated plate. The gradient of temperature between the base and the top of the bubble generates plumes at the base that move up their surfaces. These plumes give rise to eddies that survive for several minutes eventually creating a two-dimensional turbulent thermal convective flow. Our method consists in defining an appropriate stereographic projection in order to use classical numerical scheme defined for two-dimensional Navier-Stokes equations. The results are then analyzed through spherical harmonics decompositions and compared to data obtained with real soap bubble experiments.

Keywords: Computational Fluid Dynamics, Turbulence Modeling, Thermal Convection, Stereographic Projection.

1 Introduction

Two-dimensional equations are often used as a model for describing the turbulence in the atmosphere [1, 2]. Indeed, atmospheric phenomena are confined in a layer of fluid whose dimensions are only few kilometers in the vertical direction and few thousands of kilometers in the horizontal directions. This implies that most of the kinetic energy of large-scale structures is actually embedded in the horizontal velocities, the vertical component of the velocity being particularly small. Even if this modelization cannot completely describe the complexity of the atmosphere, two dimensional simulations can still be used to mimic large-scale structures motion in the atmosphere. Quite recently H. Kellay et. al [3, 4] designed a new physical experiment: a thermal convection cell composed by a half soap bubble heated at the equator. This device allowed them to study thermal convection and the movement of vortices on the surface of the bubble. They observed the emergence and persistence of isolated vortices that emerge randomly from the equator, grow in size rapidly and persist for relatively long times. They compared the motion of these vortices to hurricane trajectories on Earth and they could show that their isolated vortices and the hurricanes displayed very similar power law scaling.
The purpose of the present paper is to implement the numerical simulations corresponding to their thermal convection cell. Using a stereographic transform, we can project the Navier-Stokes equations onto a plane and use regular cartesian grid based methods to numerically solve the equations. The model is described in part 2, the numerical methods are described in part 3 and the results are analyzed and commented in part 4.

2 The model

The equations for the two-dimensional thermal convection under the Boussinesq approximation can be written as:

$$\begin{cases} \dfrac{D\mathbf{u}}{Dt} = -\dfrac{1}{\rho}\nabla p + \nu\nabla^2\mathbf{u} - \beta T\mathbf{g} \\ \nabla\cdot\mathbf{u} = 0 \\ \dfrac{DT}{Dt} = \alpha\Delta T \end{cases} \tag{1}$$

where $\dfrac{D.}{Dt} \equiv \dfrac{\partial .}{\partial t} + (\mathbf{u}\cdot\nabla).$ is the total time derivative, $\mathbf{u} = (u, v)$ denotes the velocity, p the pressure, ρ the mass density, ν the kinematic viscosity, β the coefficient of thermal expansion, $\mathbf{g}$ the gravity field, T the temperature of the fluid and α the coefficient of thermal diffusity.

3 Description of the numerical methods

3.1 The stereographic projection

The stereographic projection is a particular mapping that allows us to project a sphere onto a plane. The original projection is defined on the entire sphere, but we use in this study a version restricted to the hemisphere. This mapping is bijective and preserves the angles: a cartesian grid on the plane corresponds to a cartesian grid on the surface of the sphere. However, this particular mapping is neither isometric nor area-preserving: the distances and the areas are not preserved.

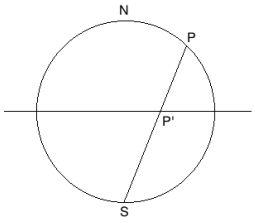

Figure 1: Stereographic projection: The point P on the sphere is projected on P' on the plane. N and S denote respectively the north and south poles.

In cartesian coordinates, if one denotes the coordinates on the sphere by (X, Y, Z) and the coordinates on the plane by (x, y), the projection and its inverse are given by the formula:

$$\begin{cases} (x, y) = \left(\dfrac{X}{1+X}, \dfrac{Y}{1+Z}\right) \\ (X, Y, Z) = \left(\dfrac{2x}{1+x^2+y^2}, \dfrac{2y}{1+x^2+y^2}, \dfrac{1-x^2-y^2}{1+x^2+y^2}\right). \end{cases} \tag{2}$$

The radius of the sphere is equal to one in these formula and in the sequel. In Figure 1, the point P on the sphere is projected on P' on the plane.

The equations (1) can thus be projected on a plane using these formula (2). The Navier-Stokes equations

projected on the plane become:

$$\begin{cases} \dfrac{\partial u}{\partial t} + \left(\dfrac{1+x^2+y^2}{2}\right)\left(u\dfrac{\partial u}{\partial x} + v\dfrac{\partial u}{\partial y}\right) + v\,(xv - yu) = \\ \qquad \nu\left[\dfrac{(1+x^2+y^2)^2}{4}\left(\dfrac{\partial^2 u}{\partial x^2} + \dfrac{\partial^2 u}{\partial y^2}\right) - (x^2+y^2)u - y(1+x^2+y^2)\dfrac{\partial v}{\partial x} + x(1+x^2+y^2)\dfrac{\partial v}{\partial y}\right] \\ \qquad\qquad -\dfrac{1}{\rho}\left(\dfrac{1+x^2+y^2}{2}\right)\dfrac{\partial p}{\partial x} - \dfrac{2x}{1+x^2+y^2}\beta g T. \\ \dfrac{\partial v}{\partial t} + \left(\dfrac{1+x^2+y^2}{2}\right)\left(u\dfrac{\partial v}{\partial x} + v\dfrac{\partial v}{\partial y}\right) - u\,(xv - yu) = \\ \qquad \nu\left[\dfrac{(1+x^2+y^2)^2}{4}\left(\dfrac{\partial^2 v}{\partial x^2} + \dfrac{\partial^2 v}{\partial y^2}\right) - (x^2+y^2)v + y(1+x^2+y^2)\dfrac{\partial u}{\partial x} - x(1+x^2+y^2)\dfrac{\partial u}{\partial y}\right] \\ \qquad\qquad -\dfrac{1}{\rho}\left(\dfrac{1+x^2+y^2}{2}\right)\dfrac{\partial p}{\partial y} - \dfrac{2y}{1+x^2+y^2}\beta g T. \end{cases} \tag{3}$$

$$\frac{\partial u}{\partial x} + \frac{\partial v}{\partial y} = \frac{2\,(xu+yv)}{1+x^2+y^2} \tag{4}$$

$$\frac{\partial T}{\partial t} + \left(\frac{1+x^2+y^2}{2}\right)\left(u\frac{\partial T}{\partial x} + v\frac{\partial T}{\partial x}\right) = \alpha\frac{(1+x^2+y^2)^2}{4}\left(\frac{\partial^2 T}{\partial x^2} + \frac{\partial^2 T}{\partial y^2}\right). \tag{5}$$

3.2 The numerical approximations

Finite differences schemes are used for solving the equations described in the previous part. The spatial domain is discretized with a staggered uniform Cartesian grid with a mesh size $h = \delta x = \delta y$, where δx and δy are the discretization steps in each direction on the projection plane. The time interval is partitioned with an uniform time steps δt. A second-order Gear scheme is used to solve the unsteady term in the governing equations. The linear terms are solved using an implicit scheme, whereas the convection terms are solved using an explicit one. If one denotes by $\mathbf{u}^n$ the approximation of $\mathbf{u}$ at time $t_n = n\delta t$, then the approximation of the total time derivative of a general variable ϕ using the second-order Gear scheme can be written as:

$$\frac{D\phi}{Dt} \approx \frac{3\phi^n}{2\delta t} - \frac{4\phi^{n-1} - \phi^{n-2}}{2\delta t} + 2(\mathbf{u}^{n-1}\cdot\nabla)\phi^{n-1} - (\mathbf{u}^{n-2}\cdot\nabla)\phi^{n-2} \tag{6}$$

The discrete values of the pressure p and the temperature T are located at the center of each cell and the discrete values of the velocity field are located at the middle of the cell sides as shown on figure 2.

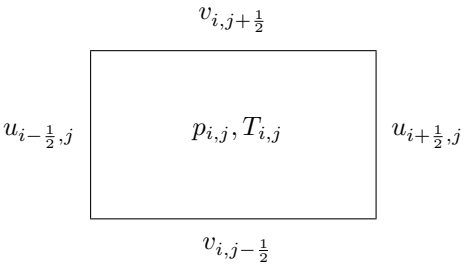

Figure 2: A staggered cell

The convection terms are approximated by a third-order Murman like scheme. A detailed study of this kind of scheme can be found in [5]. Since the temperature equation can be solved separately, a time splitting has been used to first solve the temperature equation and then the coupled pressure and velocity equations. Both of them are solved in a parallel way in a cluster by Message Passing Interface (MPI).

The discretization of the temperature equation leads to a linear system of equations $AT = E$, where A is

a pentadiagonal matrix, T is the temperature vector and E is the explicit part of the discretized temperature equation. However, the matrix A is not a self-adjoint matrix anymore in our present curved surface problem and we have to solve this linear problem using a biconjugated gradient method.

The discretization of the coupled velocity-pressure system of equations yields to solve a discrete linear system $L_h V_h^n = B_h^{n-1}$ where L_h represents the discrete operator, B_h^{n-1} is the discrete equivalent of the right hand side of (6) and $V_h^n = (\mathbf{u}_h^n, p_h^{n+1/2})$ is the approximate solution we are looking for. This discrete velocity-pressure system is solved using a V-cycle multigrid solver on a sequence of grids from G_p the finest grid to G_1, the 4×4 cells coarsest grid. The m level finest grids are partitioned to many small zones in order to use the MPI parallel computations. The other coarsest grids are solved by every core. The parallel multigrid algorithm uses a V-cycle procedure illustrated below for the computation of the fine grid solution V_h^n also denoted V_p^n in the algorithm and corresponding to the solution on the grid G_p.

$$
\begin{cases}
\text{For k=1 to number\_of\_V-cycles do} \\
\tilde{V}_p^k = S_p^{(\nu_1)}(L_p, V_p^{k-1}, B_p^{n-1}) \\
\text{Correction on coarse grids} \\
\quad \begin{cases}
\text{For q=p-1,1,-1 do} \\
\text{If q=p-m-1, collect the results of } G_{p-m} \\
\overline{V}_q^k = R_q^{q+1} \tilde{V}_{q+1}^k \\
B_q^k = R_q^{q+1}(B_{q+1}^k - L_{q+1}\tilde{V}_{q+1}^k) + L_q \overline{V}_q^k \\
\tilde{V}_q^k = S_q^{(\nu_1)}(L_q, \overline{V}_q^k, B_q^k)
\end{cases} \\
\text{Updating of the fine grids} \\
\quad \begin{cases}
\text{For q=2,p do} \\
\text{If q=p-m, partition and send out the results of } G_{p-m} \\
\hat{V}_q^k = \tilde{V}_q^k + P_{q-1}^q(V_{q-1}^k - \overline{V}_{q-1}^k) \\
V_q^k = S_q^{(\nu_2)}(L_q, \hat{V}_q^k, B_q^k)
\end{cases} \\
\text{Convergence test} \\
if\ ||B_p^{n-1} - L_p V_p^k|| \leq \xi \ \text{ stop iterations}
\end{cases}
$$

In this algorithm, $S_q^{(\nu)}$ denotes the smoothing operator used on grid G_q to compute an approximate solution of the linear system doing ν iterations. The restriction R_q^{q+1} and prolongation P_{q-1}^q operators describe the linear operators from fine-to-coarse and coarse-to-fine grids respectively. The smoothing operator S performs ν_1 or ν_2 iterations of a Gauss-Seidel cell-by-cell procedure that leads to solve a 5×5 linear system corresponding to the 5 unknowns in a cell [5].

We have performed a grid convergence analysis in order to verify that the finest grid is dense enough to describe a turbulent flow. We have computed the global temperature on the bubble for different sizes of the finest grid and for a Rayleigh number equal to 10^8. The results obtained with the 1024×1024 and 2048×2048 are almost exactly the same, whereas the results obtained with coarsest grids (256×256 and 512×512) are slightly different. The grid 1024×1024 has thus been chosen in the sequel for analyzing the other aspects of the method .

The efficiency of the parallelization process is crucial in order to improve the computational times. We can define the efficiency of the parallelization procedure by $E = \dfrac{t_1}{n \cdot t_n}$, where t_1 is the real computational time using one core and t_n is the real time cost using n cores. For instance, the efficiency evaluated for the case $m = 5$ with 1024×1024 cells is listed in table 1. A super-linear speedup is achieved for all the tests with different number of cores.

n	1	2	4	8	16
E	1	1.023	1.145	1.050	1.011

Table 1: Parallel efficiency of the numerical code for $m = 5$ with 1024×1024 cells.

4 Numerical results and analysis

The results obtained for our numerical simulations can be analyzed using mathematical tools specifically designed for spherical problems. We first recall the definitions of the spherical harmonics decompositions and then use them for computing various physical indicators (spectra and fluxes).

4.1 Spherical harmonics decompositions

Any function with spherical symmetry can be easily written as a linear combination of special functions $\{Y_l^m\}$,

$$f(\theta,\varphi) = \sum_{l=0}^{+\infty} \sum_{m=-l}^{+l} f_l^m Y_l^m(\theta,\varphi), \tag{7}$$

the so-called spherical harmonics defined by:

$$Y_l^m(\theta,\varphi) = \sqrt{\frac{2l+1}{4\pi}\frac{(l-m)!}{(l+m)!}} P_l^m\left(\cos(\theta)\right) e^{im\varphi}. \tag{8}$$

Here, $P_l^m(.)$ denotes the associated Legendre polynomials. The expansion coefficients f_l^m are then obtained by projection of f onto the spherical harmonics:

$$\begin{aligned} f_l^m &= \int_0^{2\pi}\int_0^{\pi/2} f(\theta,\varphi)\overline{Y_l^m(\theta,\varphi)}\sin(\theta)d\theta d\varphi \\ &= \sqrt{\frac{2l+1}{4\pi}\frac{(l-m)!}{(l+m)!}} \int_0^{2\pi}\int_0^{\pi/2} f(\theta,\varphi) P_l^m\left(\cos(\theta)\right) e^{-im\varphi}\sin(\theta)d\theta d\varphi \end{aligned} \tag{9}$$

The integration over φ is actually a Fourier transform and is numerically computed with a traditional FFT routine. The computations have been made using Matlab and the code is an adaptation of SpharmonicKit developed by Peter J. Kostelec [6]. The power spectrum can then be computed from the coefficients f_l^m:

$$\|f\|^2 = \sum_{l=0}^{+\infty} f_l^2 = \sum_{l=0}^{+\infty}\sum_{m=-l}^{l} |f_l^m|^2. \tag{10}$$

The coefficients f_l^m are thus equivalent to the Fourier coefficients and the coefficients f_l are equivalent to the Fourier wavenumbers in a traditional Fourier power spectrum. The coefficients f_l^m can also be used to compute the energy and enstrophy fluxes. We recall that the energy flux is computed from the nonlinear term in the Navier-Stokes equation written in Fourier space:

$$\Pi_E(k) = \int_k^{+\infty} T_E(k')dk' \tag{11}$$

where $T_E(k)$ is the nonlinear energy transfer function and is obtained by angular integration of $\widehat{\boldsymbol{v}^*(\boldsymbol{k})}.\widehat{(\boldsymbol{v}.\nabla)\boldsymbol{v}}(\boldsymbol{k})$. Here, the symbol $\widehat{.}$ denotes the usual Fourier transform. The enstrophy flux is obtained in the same way:

$$\Pi_Z(k) = \int_k^{+\infty} T_Z(k')dk' \tag{12}$$

where $T_Z(k)$ is the enstrophy transfer function and is obtained by angular integration of $\widehat{w^*(\boldsymbol{k})}.\widehat{(\boldsymbol{v}.\nabla)w}(\boldsymbol{k})$. In our study, we replace the usual Fourier decompositions by spherical harmonics decompositions, and the angular integration of the Fourier coefficients by a summation of the spherical coefficients f_l^m over the degree $m=-l$ to $m=l$.

4.2 Analysis and comments

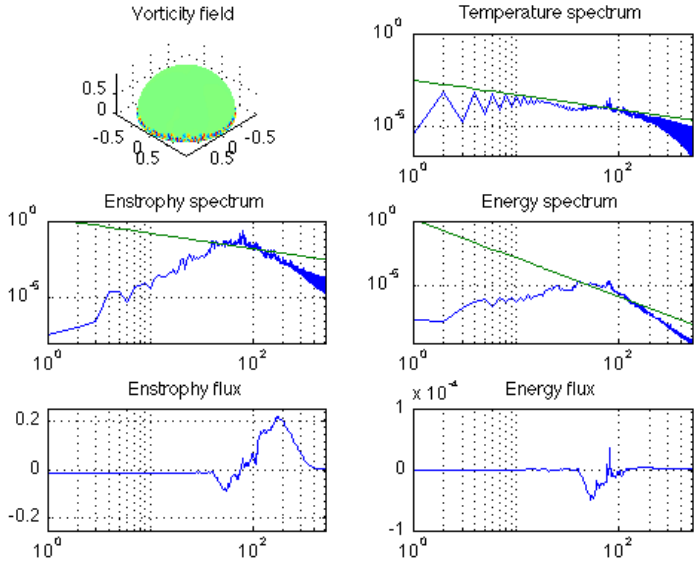

Figure 3: Numerical results in the beginning of the simulation: the curves are obtained by averaging the first ten time steps data. Indicative slopes: -0.8 for the temperature spectrum, -1 for the enstrophy spectrum and -3 for the energy spectrum

The results with a Rayleigh number $Ra = \frac{g\beta\delta T}{\nu\alpha}$ equal to 10^{-8} and a Prandtl number $Pr = \frac{\nu}{\alpha}$ equal to 7 are summarized in the figures 3, 4 and 5. Each figure is composed by a sample of the vorticity field, the temperature, enstrophy and energy spectra, and the energy and enstrophy fluxes. Figure 3 shows the results obtained in the beginning of the simulation, Figure 4 the results obtained in the middle and Figure 5 the results obtained at the end of the simulation. In the beginning of the simulations, we observe the creation of very small structures along the equator. These structures can be easily spotted on the vorticity field, and are well localized with a peak around the wavenumber 80 in the enstrophy and energy spectra. The enstrophy and energy fluxes also confirm this injection scale around 80. Short and weak cascades (inverse for the energy and direct for the enstrophy), but not yet observed in the spectra, emerge starting from the injection scale. These results are in agreement with the classical two-dimensional turbulence theory. The temperature spectrum is very small and almost flat indicating an equirepartition of temperature among the scales. We cannot observe any power law scaling in the energy spectrum nor in the enstrophy spectrum.

After a while, in the middle of the simulation (Fig. 4), we can observe large structures spreading in the vorticity field. These structures are mainly filaments, even if few isolated vortices can emerge and grow on the surface of the bubble. The small structures observed along the equator in Fig. 3 are weakening and we observe instead some kind of long plumes. A power law scaling with a -3 slope is observed in the energy spectrum. This power law scaling is confirmed in the enstrophy spectrum by a -1 power law scaling. We can also observe an upscale displacement of the enstrophy and energy fluxes. A dominant cascade of enstrophy is clearly observed, whereas the inverse cascade of energy (still present) seems to be much weaker. The temperature spectrum indicates an increase of the temperature at large scale. All these results tend to indicate an upscale motion of the injection scale which seems to be localized around the wavenumber 20.

At the end of the simulations (Fig. 5), we observe very large structures in the vorticity field. For instance, a particularly strong vortex embedded in a large positive vorticity zone can be observed in this particular snapshot. The power law scaling in the enstrophy and energy spectra are clearly observed and a dominant direct cascade of enstrophy is confirmed in the enstrophy flux. The energy flux seems to be quite unstable and does not show a clear direction. It is noticeable that the absolute value of the energy flux is very small

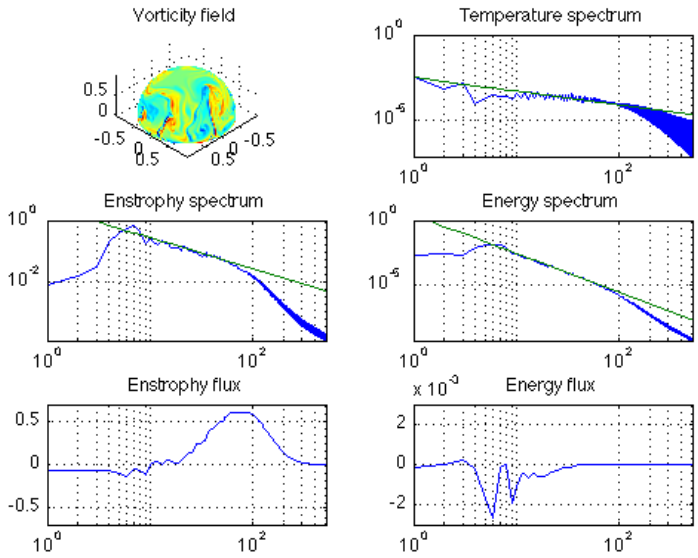

Figure 4: Numerical results in the middle of the simulation: the curves are obtained by averaging ten time steps data taken after 110 time steps. Indicative slopes: -0.8 for the temperature spectrum, -1 for the enstrophy spectrum and -3 for the energy spectrum

compared to the absolute value of the enstrophy flux. A power law scaling with a -0.8 slope is observed in the temperature spectrum. This is not really surprising since in a thermal convection cell, the temperature and the vorticity fields are very similar.

5 Conclusion

We have presented in this paper an original way of computing numerical simulations of turbulent flows on an hemisphere. The stereographic projection allows us to use regular finite difference schemes on cartesian grids. This framework also allows us to implement a multigrid approach with parallel computations. The parallelization is very efficient and we obtain a super linear speedup. Using spherical harmonics decompositions, we perform qualitative analysis of the results. We observe that the thermal convection is creating an injection scale that is growing with time. A clear direct cascade of enstrophy similar to the one predicted in the classical two-dimensional turbulence theory is created by the thermal convection [7]. The enstrophy cascade is usually observed in simulations where a low wavenumber forcing is applied so that the full resolution can be used for the enstrophy cascade. In our results, the inverse energy cascade is very weak and a -5/3 slope is not observed in the energy spectrum. This might be explained by the ever growing injection scale and the lack of a large scale dissipation term in the equations. Hypoviscosity at small wave numbers to destroy bubble-size structures, or at least a linear friction term, could be added in future simulations in order to stabilize the flow and strengthen the emergence of an inverse energy cascade. We can compare our results to the observation made by Smith and Yakhot in [8] and already predicted by Kraichnan [2]: the formation of a large scale structure akin a Bose-Einstein condensate. The main difference is that we do not observe here an inverse cascade from the injection scale to the large scales but an ever growing injection scale with time. We have also to emphasize that we do not observe a Bolgiano regime [9, 10] in our numerical simulations. An important feature of Bolgiano's theory is the interaction between gravitational potential energy and turbulent kinetic energy. For scales larger than a scale usually called the Bolgiano scale, if the buoyancy force is strong enough then the Kolmogorov -5/3 law gives way to a -11/5 scaling for the energy spectrum [11, 12]. This is obviously not observed in our results, and this is certainly due to our ever growing injection scale. These preliminary results will be extended and confirmed by further numerical simulations.

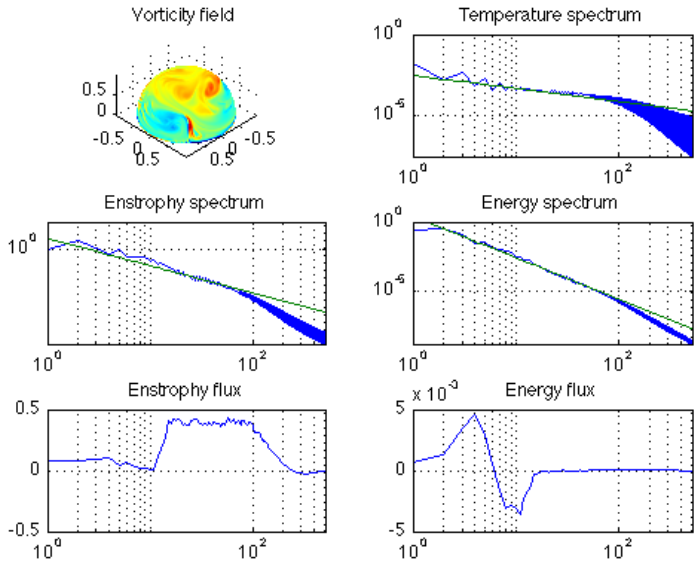

Figure 5: Numerical results at the end of the simulation: the curves are obtained by averaging ten time steps data taken after 350 time steps. Indicative slopes: -0.8 for the temperature spectrum, -1 for the enstrophy spectrum and -3 for the energy spectrum

Acknowledgments

The research is supported by the french Agence Nationale de la Recherche, under grant "Cyclobulle" funding. The authors wish to thank Hamid Kellay for very useful discussions about the physical interpretation of our results.

References

[1] R. Kraichnan and D. Montgomery. Two-dimensional turbulence. *Rep. Prog. Phys.*, 43:547–619, 1980.
[2] R. Kraichnan. Inertial ranges in two-dimensional turbulence. *Phys. Fluids*, 10:1417–1423, 1967.
[3] F. Seychelles, Y. Amarouchene, M. Bessafi, and H. Kellay. Thermal Convection and Emergence of Isolated Vortices in Soap Bubbles. *Phys. Rev. Letters*, 100(144501), 2008.
[4] F. Seychelles, F. Ingremeau, C. Pradere, and H. Kellay. From Intermittent to Nonintermittent Behavior in Two Dimensional Thermal Convection in a Soap Bubble. *Phys. Rev. Letters*, 105(264502), 2010.
[5] C.H. Bruneau and M. Saad. The 2D lid-driven cavity problem revisited. *Computers and Fluids*, 35:326–348, 2006.
[6] P. Kostelec. SpharmonicKit. [http://www.cs.dartmouth.edu/ geelong/sphere].
[7] U. Frisch. *Turbulence, The legacy of A.N. Kolmogorov*. Cambridge University Press, 1995.
[8] L. Smith and V. Yakhot. Bose condensation and small-scale structure generation in a random force driven two dimensional turbulence. *Phys. Rev. Lett.*, 64:352–355, 1993.
[9] R. Bolgiano. Turbulent spectra in a stably stratified atmosphere. *J. Geophys. Res.*, 71:2226–2229, 1959.
[10] R. Bolgiano. Structure of turbulence in stratified media. *J. Geophys. Res.*, 67(065301), 1962.
[11] X.D. Shang and K.O Xia. Scaling of the velocity power spectra in turbulent thermal convection . *Phys. Rev. E*, 64(065301), 2001.
[12] J. Zhang and X.L. Wu. Velocity intermittency in a buoyancy subrange in a two-dimensional soap film convection experiment. *Phys. Rev. Lett.*, 94(234501), 2005.